WEP Warwick Evans Publishing

International Journal of Materials Science and Technology Studies

ISSN: 3006-7693 (Print), ISSN: 3006-3744 (Online) | Volume 5, Number 2, Year 2026
DOI: https://doi.org/10.62051/ijmsts.v5n2.03
Journal homepage: https://wepub.org/index.php/IJMSTS/index

Research Progress on Photocatalysis of Lead-Free Halide Perovskite $Cs_3Bi_2X_9$ (X=I, Br, Cl)

Benhong Mu *

College of Environmental Science and Engineering, North China Electric Power University, Beijing 102206, P.R. China

*Corresponding Author: mubenhong@163.com

ABSTRACT

In recent years, the application of metal halide perovskites in the field of photocatalysis has emerged as a rapidly developing research area. However, the toxicity and stability issues of traditional lead (Pb)-containing perovskites limit their large-scale application. Therefore, the development of efficient and stable lead-free perovskite materials is one of the key current research directions. $Cs_3Bi_2X_9$ (X = I, Br, Cl), as a lead-free metal halide perovskite, offers the primary advantages of being environmentally friendly and having potentially higher stability. This article provides an overview of the application of this material system in replacing lead-based perovskites to achieve environmentally friendly photocatalysis, as well as its synthesis methods. It aims to serve as a reference for the development of efficient and stable lead-free perovskite photocatalysts.

KEYWORDS

Lead-free halide perovskite; Photocatalysis; Synthesis methods

1. INTRODUCTION

In the current energy utilization landscape, fossil fuels still dominate, but as a finite natural resource, their large-scale use not only faces the challenge of depletion but also leads to severe environmental pollution. Therefore, the development and utilization of clean energy have become a crucial direction for the global energy transition. Solar energy, an inexhaustible and renewable resource, holds the potential to fundamentally alleviate the dual pressures of energy shortage and environmental pollution through efficient and rational utilization [1-5]. Among various technologies, photocatalysis stands out as an effective means for the direct conversion and utilization of solar energy, garnering widespread attention from researchers. As a metal halide perovskite, $Cs_3Bi_2X_9$ (X=I, Br, Cl) offers core advantages, including a tunable optical bandgap, excellent visible light absorption capability, and non-toxic, environmentally friendly properties. By adjusting the halogen composition, its band structure can be precisely tuned to match various photocatalytic reactions (such as water splitting for hydrogen production, CO_2 reduction, and dye degradation), thereby enabling efficient utilization of sunlight [6-8]. Compared to lead-based perovskites, its lead-free and fully inorganic composition significantly enhances the material's environmental friendliness and chemical stability. Additionally, the material exhibits good carrier transport properties, facilitating the separation and utilization of photogenerated electron-hole pairs. These characteristics endow such materials with immense potential in the fields of solar energy conversion and environmental pollution remediation [9, 10]. However, reports on the photocatalytic applications of $Cs_3Bi_2X_9$ remain scarce. This review systematically outlines the development and applications of the lead-free perovskite material $Cs_3Bi_2X_9$ (X=I, Br, Cl) in the field of photocatalysis. It begins with a detailed enumeration of its main synthesis

methods, explaining the advantages and disadvantages of each. In terms of applications, the review focuses on the research progress of this material in photocatalytic CO_2 reduction, photocatalytic water splitting for hydrogen production, and photocatalytic degradation of organic pollutants. Specific case studies are discussed to explore strategies for enhancing its performance, such as elemental doping and heterojunction construction. Finally, the existing research findings are summarized, and future development trends are prospected.

2. SYNTHESIS METHODS OF $Cs_3Bi_2X_9$ PHOTOCATALYST

2.1. Anti-solvent Method

The Anti-solution method is the most commonly used technique for preparing $Cs_3Bi_2X_9$ materials, facilitating the control of material morphology and size. The anti-solvent method for synthesizing $Cs_3Bi_2X_9$ is simple and rapid. It involves dissolving CsX (e.g., CsI) and BiX_3 (e.g., BiI_3) in polar aprotic solvents like dimethyl sulfoxide (DMSO) or N,N-dimethylformamide (DMF) at a molar ratio of 3:2. Under stirring, this precursor solution is slowly dripped into an anti-solvent such as isopropanol (IPA). Due to its extremely low solubility in the anti-solvent, $Cs_3Bi_2X_9$ rapidly precipitates and undergoes recrystallization [11, 12]. For example, Guo et al. prepared $Cs_3Bi_2Cl_9$ quantum dots via the anti-solvent method with an average particle size of 2.59 ± 0.6 nm. Swapnil Sarkar et al. used the anti-solvent method to produce aggregated block-like $Cs_3Bi_2I_9$ [13], while Tawfik Guesmi, also using the anti-solvent method, obtained hexagonal sheet-like $Cs_3Bi_2I_9$ [14]. These variations in morphology are attributed to differences in the types and quantities of organic solvents used. Furthermore, experiments by Zhang et al. showed that different anti-solvents yield $Cs_3Bi_2I_9$ films with distinct morphologies. Films treated with toluene as the anti-solvent were more uniform, smooth, highly reflective, and exhibited the best optoelectronic performance [15]. Therefore, the anti-solvent method allows partial control over particle size by adjusting precursor concentration, dripping rate, and anti-solvent type. However, this method is prone to introducing solvent residue, and inadequate washing can adversely affect the material's properties.

2.2. Hydrothermal Method

The hydrothermal method involves dissolving CsX and BiX_3 precursors in DMF or HX acid solution, stirring to form a clear solution, and transferring the solution to a Teflon-lined high-pressure reactor. The reaction proceeds at a certain temperature (typically 120-180°C) for several to tens of hours. $Cs_3Bi_2X_9$ materials obtained via the hydrothermal method exhibit high crystallinity and controllable morphology, generally forming nanosheets or microspheres. For example, Hashimoto et al. dissolved CsBr, $BiBr_3$, CsI, and BiI_3 in 15 mL of HBr in different molar ratios, placed the mixture in a Teflon-lined reactor, reacted at 180°C for 10 hours, and finally obtained $Cs_3Bi_2Br_{9-x}I_x$ solid solutions through centrifugation and drying [16]. Additionally, by adjusting solvent composition, reaction temperature and time, and surfactants such as oleic acid, the specific surface area and exposed crystal facets of the products can be precisely controlled [17]. High crystallinity ensures good carrier mobility, while controllable nano-morphology provides a large reaction interface and abundant active sites [18]. The drawbacks of this method are also evident: it requires high-pressure equipment and has a long reaction cycle.

2.3. Hot Injection Method

Generally, the hot injection method involves separately preparing a cesium precursor (such as cesium oleate in 1-octadecene) and a bismuth precursor (such as BiX_3 with ligands in 1-octadecene) under an inert atmosphere. The bismuth precursor is heated to a specific temperature (150-180°C), and the cesium precursor is rapidly injected. This causes the system to instantly reach supersaturation, triggering uniform nucleation. The reaction typically proceeds for a few minutes before being

quenched by cooling in an ice bath. Finally, acetone is added, and the mixture is centrifuged to obtain nanocrystals [19, 20]. $Cs_3Bi_2X_9$ materials synthesized via the hot injection method exhibit small size and large specific surface area, which are beneficial for light absorption and carrier migration to the surface. Their micro-morphology often appears as nanosheets or quantum dots. For example, Lian et al. first separately prepared cesium oleate (Cs-oleate) and a bismuth precursor by mixing $BiBr_3$, oleylamine, and oleic acid in 1-octadecene. The cesium precursor was then rapidly injected into the bismuth precursor at 180°C under a nitrogen atmosphere to induce instantaneous nucleation. After completion, the reaction was quenched in an ice-water bath. The product was subsequently separated via selective centrifugation to obtain nanosheets with a parallelogram-like morphology [20]. Tang et al. added a certain ratio of cesium acetate and bismuth acetate to a mixed solution of oleic acid, oleylamine, and 1-octadecene. The mixture was heated to 120°C under nitrogen (N_2) protection and held at that temperature for 30 minutes. Subsequently, the solution temperature was raised to 150°C, followed by rapid injection of trimethylsilyl iodide (TMS-I). After the reaction, the solution was immediately cooled in an ice-water bath, yielding hexagonal sheet-like $Cs_3Bi_2I_9$ [21]. Compared to the aforementioned methods, the hot injection method is more complex, yields lower quantities, and the ligands used may cover active sites, requiring post-treatment for removal.

2.4. Grinding Method

The common grinding method involves placing CsX and BiX_3 raw materials in a high-energy ball milling tank at a 3:2 molar ratio, along with zirconia grinding balls, and conducting extended ball milling at room temperature. The energy generated from mechanical collisions directly induces solid-state ionic reactions, forming $Cs_3Bi_2X_9$ material [22]. Notably, Leunam et al. prepared $Cs_3Bi_2Br_9$ using a planetary ball mill in ambient air at a constant speed of 700 rpm, with different milling durations (0, 1, 3, 5, 7, 12 hours) at room temperature. Analysis of samples extracted at each time point revealed that the perovskite phase of $Cs_3Bi_2Br_9$ had largely formed within 1 hour of milling. However, when milling was extended to 12 hours, XPS analysis indicated partial decomposition of the material, with the reappearance of precursor phases, suggesting structural degradation under sustained mechanical stress [23]. Additionally, Feng et al. manually ground $BiBr_3$ and CsBr in a mortar without any organic solvents or surfactants, resulting in the preparation of ultrathin hexagonal $Cs_3Bi_2Br_9$ nanosheets. During the grinding process, $BiBr_3$ adsorbed trace moisture from the air, undergoing incomplete hydrolysis to form $Bi(OH)_3$ nanoparticles and a small amount of hydrobromic acid solution. This facilitated the formation of the nanosheet structure and promoted ion diffusion. Subsequently, $Bi(OH)_3$ acted as nucleation sites, combining with CsBr to self-assemble into $Cs_3Bi_2Br_9$ at room temperature [24]. While the grinding method is relatively simple and environmentally friendly, the resulting material's microscopic morphology can be irregular. For instance, Niyitanga et al. synthesized $Cs_3Bi_2I_9$ by grinding precursor CsI and BiI_3 in a mortar, yielding a material with irregular granular morphology [25]. Moreover, the grinding process tends to introduce more defects in the material, which may be beneficial for certain photocatalytic reactions. Therefore, a trade-off between crystallinity and defect density must be considered during material preparation.

3. APPLICATIONS OF $CS_3BI_2X_9$ IN THE FIELD OF PHOTOCATALYSIS

3.1. Photocatalytic Reduction Of CO_2

With the industrialization and increasing energy consumption of human society, CO_2 emissions have risen sharply, leading to global climate change and environmental issues. Consequently, finding effective methods for CO_2 reduction has become crucial. Photocatalytic reduction of CO_2 utilizes solar energy to convert CO_2 into valuable chemical fuels (such as methane, carbon monoxide, and formic acid) [26]. When a photocatalyst absorbs sunlight, it generates reducing electrons and oxidizing holes. After separation and migration, the photogenerated electrons migrate to the catalyst

surface for reducing CO_2, while the holes are typically used to oxidize water molecules or other sacrificial agents, providing protons (H^+) to maintain charge balance. Notably, water splitting is a competing reaction within the photocatalytic system, so seeking material synthesis strategies to overcome this challenge is essential for improving photocatalytic performance [27, 28]. Feng et al. synthesized ultrathin $Cs_3Bi_2Br_9$ nanosheets via grinding under specific humidity conditions and incorporated Cu into the $Cs_3Bi_2Br_9$ lattice. Cu doping enhanced the light absorption intensity of the catalyst and altered its electronic structure. This modified the electron cloud delocalization at the Bi adsorption sites, thereby lowering the energy barrier for the CO_2-to-CO conversion, as shown in Figure 1 (a) and (b). The CO selectivity increased from 58.16% ($Cs_3Bi_2Br_9$ NPs) to 98.60% ($Cs_3Bi_2Br_9$/5%Cu NPs) [24]. Ren et al. constructed a 0D/2D BiOBr/ $Cs_3Bi_2Br_9$ (CBB) heterojunction photocatalyst using an in-situ growth strategy. Experimental characterization and DFT calculations revealed that BiOBr/CBB conforms to an S-scheme heterojunction band structure. This configuration enhanced carrier separation efficiency and the redox capability of the catalyst. Using water as an electron donor, the heterojunction achieved CO_2 reduction, yielding CO, CH_4 and H_2. The optimized CBB/BOB heterojunction exhibited excellent activity and CH_4 selectivity. The CH_4 production rate and selectivity were 12.8 $\mu mol \cdot g^{-1} \cdot h^{-1}$ and 79%, respectively, representing a 43-fold increase in production rate and a 2-fold increase in selectivity compared to the pure CBB material [12]. Liu et al. constructed a $Cs_3Bi_2Br_9/Bi_{19}Br_3S_{27}$ Z-scheme heterojunction via an in-situ growth method. The constructed heterojunction exhibited a broader light absorption range, particularly in the near-infrared region. The increased light absorption range, improved carrier separation efficiency, and enhanced redox capability contributed to its excellent CO_2 reduction performance, as shown in Figure 1 (c)-(e). The heterojunction achieved production rates of 123 $\mu mol \cdot g^{-1} \cdot h^{-1}$ for CH_4 and 17 $\mu mol \cdot g^{-1} \cdot h^{-1}$ for CO, which were 70 times and 124 times higher than those of pristine $Cs_3Bi_2Br_9$ and $Bi_{19}Br_3S_{27}$, respectively [29]. Bhosale et al. first ground BiI_3 with CsI to form bulk perovskite, followed by ultrasonic fragmentation and surface passivation using oleic acid (OA) and oleylamine (OLA), ultimately obtaining $Cs_3Bi_2I_9$ nanocrystals with a size of approximately 6.2 nm. After 10 hours of UV illumination at the gas-solid interface, $Cs_3Bi_2I_9$ demonstrated excellent CO generation capability reaching 77.6 μmol/g, alongside a methane yield of 14.9 μmol/g. Infrared spectroscopy indicated that $Cs_3Bi_2I_9$ primarily catalyzes CO_2 reduction via a bidentate pathway. Specifically, CO_2 adsorbs onto Lewis acid sites of the BiI_6 octahedra, proceeds through a bridging/bidentate carbonate intermediate to form formate, and is ultimately converted to CO and CH_4 [30]. Quintero-Lizárraga et al. immobilized $Cs_3Bi_2I_9$ perovskite on two different substrates using thin-film deposition and porous structure encapsulation techniques, respectively. The perovskite on the two substrates exhibited distinct morphologies: clear hexagonal particles formed on mica, while porous concrete promoted the formation of needle-shaped particles. This approach not only significantly enhanced its activity and efficiency in the photocatalytic reduction of CO_2 to formic acid, achieving a yield of 2570 μmol, but also improved the material's stability in aqueous environments and at high temperatures [31].

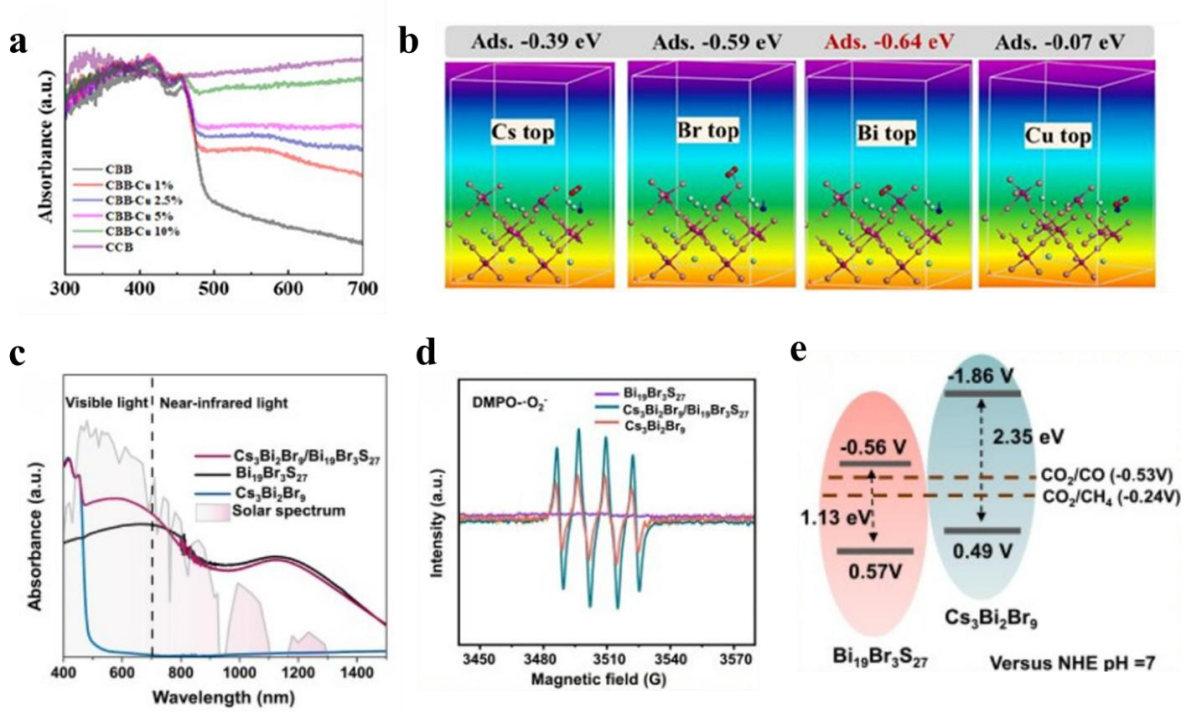

Figure 1. (a) UV–vis diffuse reflection spectra of the samples. (b) Optimized atomic configurations of CO_2 adsorption site and the corresponding Eads of CBB/5 % Cu NPs: Cs top, Br top, Bi top and Cu top, respectively [24]. (c) UV–vis-NIR DRS spectra of $Cs_3Bi_2Br_9$, $Bi_{19}Br_3S_{27}$ and $Cs_3Bi_2Br_9$/ $Bi_{19}Br_3S_{27}$ heterojunction. (d) ESR spectra of $Cs_3Bi_2Br_9$, $Bi_{19}Br_3S_{27}$ and $Cs_3Bi_2Br_9$ heterojunction. (e) Energy band position diagram of $Cs_3Bi_2Br_9$ and $Bi_{19}Br_3S_{27}$ (versus NHE at pH = 7) [29].

3.2. Photocatalytic Hydrogen Production

Semiconductor materials absorb sunlight, generating separable electrons and holes upon photoexcitation, and drive them to migrate to the material surface. This allows the electrons and holes to participate in the reduction and oxidation reactions of water, respectively. To drive the redox reaction of water splitting, the valence band (VB) of the semiconductor should be more positive than the potential for oxidizing H_2O to O_2 (1.23 V vs. Normal Hydrogen Electrode (NHE) at pH = 0), while the conduction band (CB) of the semiconductor should be more negative than the potential for reducing H^+ to H_2 (0 V vs. NHE at pH = 0) [32]. The CB potential of $Cs_3Bi_2X_9$ is more negative than the H^+/H_2 reduction potential, satisfying the thermodynamic requirement for water reduction. Theoretically, some metal halide perovskites (MHPs) can also oxidize water to generate O_2, as their VB potentials are relatively positive. Medina-Llamas et al. formed a Type-II heterojunction between $Cs_3Bi_2Br_9$ nanocrystals and g-C_3N_4 nanosheets. The VB energy level of g-C_3N_4 is more positive than that of $Cs_3Bi_2Br_9$. Therefore, the holes (h^+) generated on g-C_3N_4 spontaneously migrate to the valence band of $Cs_3Bi_2Br_9$. Simultaneously, the conduction band (CB) energy level of $Cs_3Bi_2Br_9$ is more negative than that of g-C_3N_4. Consequently, the electrons (e^-) excited on $Cs_3Bi_2Br_9$ migrate to the conduction band of g-C_3N_4. The electrons ultimately accumulate on the g-C_3N_4 nanosheets, where they are captured by pre-deposited Pt cocatalysts, leading to hydrogen generation. The holes, on the other hand, accumulate on the $Cs_3Bi_2Br_9$ nanocrystals and are consumed by the sacrificial agent triethanolamine (TEOA), preventing electron-hole recombination. When the loading of $Cs_3Bi_2Br_9$ nanocrystals was 0.02 wt.%, the hydrogen production rate of the heterojunction material reached 4593 $\mu mol \cdot g^{-1} \cdot h^{-1}$, representing a 43% improvement compared to pure g-C_3N_4 nanosheets (3212 $\mu mol \cdot g^{-1} \cdot h^{-1}$) [33]. Xia et al. fabricated a Z-scheme heterojunction of $Cs_3Bi_2Br_9/FeS_2$ (CBB/FS) via a simple electrostatic self-assembly method. Under light irradiation, both CBB and FS generate e^- and h^+. Electrons from the CB of CBB rapidly transfer to the VB of FS and recombine with the holes in FS, as shown in Figure. 2 (a). This process retains the highly reductive electrons on the CB of FS and the

strongly oxidative holes on the VB of CBB. The construction of the Z-scheme heterojunction not only achieves efficient charge separation but also preserves the strong redox capability of the carriers. Furthermore, FS possesses full-spectrum absorption capability, especially strong absorption in the near-infrared region. This not only improves light utilization but also converts light energy into heat, raising the reaction system temperature from 12.6°C to 54.8°C within 20 minutes, as shown in Figure. 2 (b). The temperature increase accelerates carrier migration rates and lowers the reaction energy barrier for photocatalytic hydrogen production. The prepared CBB/FS-5 composite exhibited a high hydrogen production rate of 31.5 $mmol \cdot g^{-1} \cdot h^{-1}$ [34]. Fan et al. loaded negatively charged MoS_2 quantum dots (QDs) onto positively charged $Cs_3Bi_2I_9$ surfaces via electrostatic self-assembly, forming MoS_2 QDs/ $Cs_3Bi_2I_9$ heterojunction composites. This heterojunction conforms to the Type-II charge separation mechanism, as shown in Figure. 2 (c). Under illumination, photogenerated electrons from $Cs_3Bi_2I_9$ efficiently migrate to the MoS_2 QDs, where they participate in proton reduction at the active sites of MoS_2 QDs to generate hydrogen. This achieves spatial charge separation and significantly enhances photocatalytic efficiency. The optimal hydrogen evolution performance reached 6.09 $mmol \cdot g^{-1} \cdot h^{-1}$ with a MoS_2 QDs loading of 5.4 wt% [35]. Mutairah S. et al. constructed a composite material termed CBISB/rGO, whose structure can be understood as a "bridge" configuration. In this composite, $Cs_3Bi_2I_9$ is responsible for efficiently capturing visible light and generating photogenerated carriers. Sb_2O_3 provides oxidation capability and chemical stability. The incorporation of reduced graphene oxide (rGO) addresses the poor conductivity of $Cs_3Bi_2I_9$ and facilitates rapid transport of photogenerated electrons within the material, thereby suppressing electron-hole recombination and substantially improving overall photocatalytic efficiency. Under visible light irradiation, this composite material achieved a hydrogen production rate of 700 $\mu mol \cdot g^{-1}$ at 120 minutes [36].

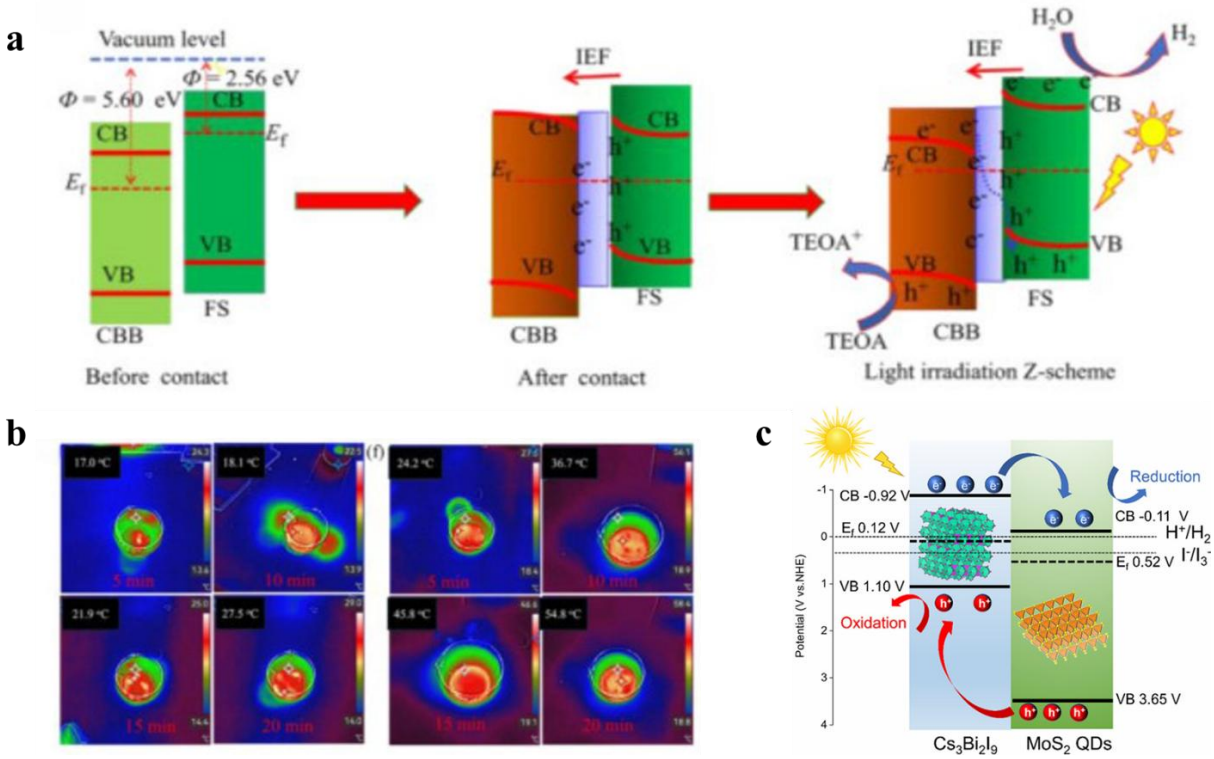

Figure 2. (a) Schematic illustration of the band structures of CBB and FS (left), interfacial charge transfer and the formation of an IEF upon heterojunction (middle), and schematic of CBB/FS for photocatalytic H_2 production and illustration of the charge transfer process of the photogenerated electrons (right). (b) H_2 evolution rates of CBB and CBB/FS-5 under different temperatures. Photothermal-assisted infrared temperature distributions for CBB and CBB/FS-5 samples under different irradiation time intervals [34]. (c) Schematic band diagram of $Cs_3Bi_2I_9$ and MoS_2 QDs for photo catalytic HI splitting reactions [35].

3.3. Photocatalytic Degradation Of Dyes

Common dye wastewater includes substances like methylene blue (MB) and rhodamine B (RhB). When dye wastewater is mixed with a $Cs_3Bi_2X_9$ photocatalyst, dye molecules adsorb onto the catalyst particle surfaces through electrostatic interactions, van der Waals forces, or hydrogen bonds. When the incident light energy exceeds the bandgap energy of the $Cs_3Bi_2X_9$ photocatalyst, photogenerated electrons (e^-) and holes (h^+) are created. Driven by the internal electric field and diffusion within the material, they migrate towards the catalyst surface. Electrons that reach the surface are captured by adsorbed oxygen molecules, undergoing a multi-step reduction process: $e^- + O_2 \rightarrow \cdot O_2^-$. The superoxide radical ($\cdot O_2^-$) further reacts with H^+ to generate intermediates like hydrogen peroxide (H_2O_2), ultimately producing highly reactive hydroxyl radicals (·OH). Meanwhile, holes can directly oxidize dye molecules adsorbed on the catalyst surface, causing the dye to lose electrons and degrade. Additionally, holes can react with water molecules or hydroxide ions adsorbed on the catalyst surface to generate hydroxyl radicals: $h^+ + H_2O \rightarrow \cdot OH + H^+$, $h^+ + OH^- \rightarrow \cdot OH$ [37, 38]. The generated ·OH and $\cdot O_2^-$ radicals possess extremely strong and non-selective oxidizing power, which can significantly enhance the degradation efficiency of dye wastewater by $Cs_3Bi_2X_9$. These highly active ·OH and $\cdot O_2^-$ radicals attack the chromophores of the dye molecules. Once the chromophores are destroyed, the color of the dye wastewater gradually fades. As the reaction proceeds, structures like aromatic rings are cleaved by ·OH and other species, forming small-molecule organic acids such as aliphatic carboxylic acids, aldehydes, and ketones. These small intermediate products are further oxidized, with carbon chains continuously breaking. Ultimately, the carbon in the organic compounds is converted to CO_2, hydrogen to H_2O, and heteroatoms like nitrogen, sulfur, and phosphorus are transformed into inorganic ions (e.g., NO_3^-, SO_4^{2-}, PO_4^{3-}) [39-41]. O. Akinbami et al. synthesized $Cs_3Bi_2Br_9$ nanoparticles using the hot injection method. Under simulated sunlight irradiation, $Cs_3Bi_2Br_9$ nanoparticles demonstrated strong degradation capabilities for both Rhodamine B and Methylene Blue dyes. Within 100 minutes, Rhodamine B was completely degraded (100%), and the degradation rate for Methylene Blue reached 99.3%, as shown in Figure. 3 (a)-(c). The primary degradation pathway for Rhodamine B involves a stepwise deethylation process, where the ethyl groups ($-CH_2CH_3$) on the side chains of the RhB molecule are removed one by one, generating a series of intermediate products. The main degradation pathway for Methylene Blue involves demethylation, with the methyl groups ($-CH_3$) on the MB molecule being progressively removed, as shown in Figure. 3 (d) and (e) [42]. Bresolin et al. successfully synthesized $Cs_3Bi_2I_9$ powder via a low-temperature solvothermal method. After 180 minutes of visible light irradiation, the degradation rate of RhB by $Cs_3Bi_2I_9$ reached 93%. After three cycles of reuse, the catalyst's activity only slightly decreased (from 93% to 92%), demonstrating good reusability [43].

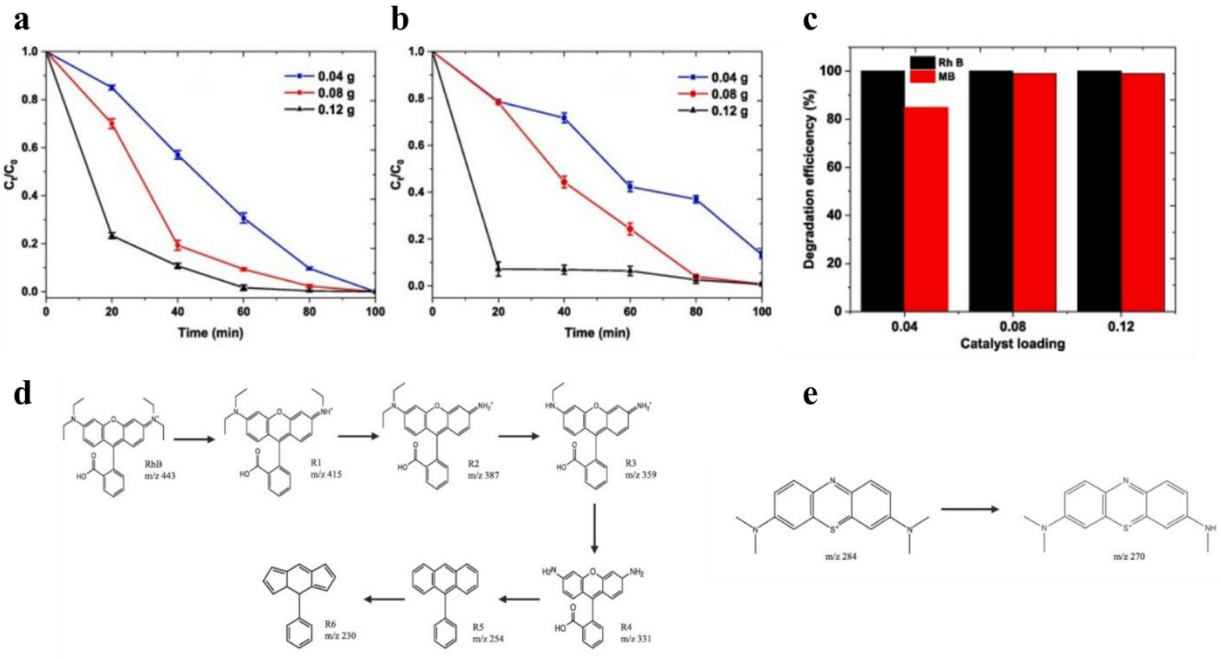

Figure 3. (a) Effect of $Cs_3Bi_2Br_9$ photocatalyst load: variation of C_t/C_0 during photodegradation (a) RhB, (b) MB dyes and (c) photodegradation efficiency of $Cs_3Bi_2Br_9$ after 100 min. Degradation products of (d) RhB (e) MB determined by mass spectrometry [42].

4. CONCLUSION AND PROSPECT

In recent years, addressing the toxicity and stability concerns of traditional lead-based perovskites, lead-free perovskite $Cs_3Bi_2X_9$ (X=I, Br, Cl) has emerged as a research hotspot in the field of photocatalysis due to its non-toxicity, tunable bandgap, and excellent optoelectronic properties. Synthesis methods such as the anti-solvent method, hydrothermal method, hot injection method, and grinding method each have distinct characteristics. Studies have shown that strategies like elemental doping and heterojunction construction can significantly enhance its performance and selectivity in photocatalytic CO_2 reduction, hydrogen production, and degradation of organic pollutants. Despite the promising prospects, this field still faces challenges. Future research should focus on elucidating the underlying photocatalytic mechanisms in greater depth and addressing the long-term stability of the material in complex environments, especially in aqueous phases. Further optimization of the material's microstructure (e.g., morphology, defect engineering) and the development of multi-component solid solutions are expected to achieve fine-tuning of its properties. Simultaneously, exploring its applications in new reaction systems and advancing the transition of the material from laboratory powder catalysts to practical macroscopic structured devices are crucial for its large-scale application.

REFERENCES

[1] Sun, C., et al., Water-stable Bi-based perovskite for efficient photocatalytic hydrogen evolution in aqueous media. Journal of Colloid and Interface Science, 2026. 709: p. 10.

[2] Li, M., et al., Dual-functional Cs_2CuBr_4@ZnO S-scheme heterojunction photocatalyst for efficient organic pollutant degradation and toluene oxidation. Journal of Colloid and Interface Science, 2026. 708: p. 11.

[3] Omer, W., et al., Water-stable halide perovskite nanocomposite with dual S-scheme for enhanced photocatalysis. Journal of Industrial and Engineering Chemistry, 2026. 155: p. 407–419.

[4] Jena, A., A. Kulkarni, and T. Miyasaka, Halide Perovskite Photovoltaics: Background, Status, and Future Prospects. Chemical Reviews, 2019. 119(5): p. 3036–3103.

[5] Ke, W. and M. Kanatzidis, Prospects for low-toxicity lead-free perovskite solar cells. Nature Communications, 2019. 10: p. 4.

[6] Poli, I., et al., Lead-free perovskites and derivatives for photogeneration: a roadmap to sustainable approaches for photovoltaics and photo(electro)catalysis. Journal of Physics-Energy, 2026. 8(1): p. 56.

[7] Li, C., et al., Perovskite materials for multifaceted energy applications: From fundamental properties to industrialization challenges. Materials Science in Semiconductor Processing, 2026. 202: p. 21.

[8] Boretti, A., Advances and prospects of lead-free metal halide perovskites for solar hydrogen fuel generation. Transition Metal Chemistry, 2026. 51(2): p. 21.

[9] Xiao, Z., Z. Song, and Y. Yan, From Lead Halide Perovskites to Lead-Free Metal Halide Perovskites and Perovskite Derivatives. Advanced Materials, 2019. 31(47): p. 22.

[10] Huang, H., et al., Lead Halide Perovskite Nanocrystals in the Research Spotlight: Stability and Defect Tolerance. Acs Energy Letters, 2017. 2(9): p. 2071–2083.

[11] Zheng, Y., et al., Lead-free perovskite $Cs_3Bi_2Br_9/TiO_2$ composites for atmospheric photocatalytic oxidation of sulfides. Green Chemistry, 2024. 26(12): p. 7031–7037.

[12] Ren, A., et al., Constructing S-scheme heterojunction $Cs_3Bi_2Br_9$/BiOBr via in-situ partial conversion to boost photocatalytic N_2 fixation. Journal of Colloid and Interface Science, 2025. 678: p. 1203–1212.

[13] Sarkar, S., T. Bhoyar, and S. Umare, $Cs_3Bi_2I_9$ embedded polymeric carbon nitride photocatalyst for hexavalent chromium reduction and acid violet 7 degradation. Materials Today Communications, 2025. 49: p. 13.

[14] Guesmi, T., et al., Optimization of the photocatalytic wastewater treatment process via a response surface methodology-central composite design strategy and CO_2 reduction using a novel $Cs_3Bi_2I_9/Ag_3PO_4$ composite under visible light. Journal of Water Process Engineering, 2025. 78: p. 18.

[15] Zhang, Y., et al., Synthesis of cesium bismuth iodide perovskite using toluene as anti-solvent with higher photocurrent response. Materials Letters, 2022. 310: p. 4.

[16] Hashimoto, H., et al., Bandgap and Photoluminescence Tunability of Lead-Free $Cs_3Bi_2(Br,I)_9$ Solid Solution Compounds. Physica Status Solidi-Rapid Research Letters, 2024. 18(9): p. 6.

[17] Liu, J., et al., Synaptic plasticity and handwritten digit recognition of a memristor based on a high-stability lead-free $Cs_3Bi_2Br_9$ perovskite thin film. Journal of Materials Chemistry C, 2025. 13(16): p. 8084–8094.

[18] Wang, H., et al., Lead-Free Perovskite $Cs_3Bi_2Br_9$/Porous BiOCl S-Scheme Heterostructure with Greatly Enhanced Performance for CO_2 Reduction. Acs Applied Materials & Interfaces, 2025. 17(27): p. 39218–39225.

[19] Hai, O., et al., K plus -doped lead-free $Cs_3Bi_2Br_9$ nanocrystals Enable efficient blue emission and Ultra-stability. Ceramics International, 2025. 51(4): p. 5053–5060.

[20] Lian, L., et al., Colloidal synthesis of lead-free all-inorganic cesium bismuth bromide perovskite nanoplatelets. Crystengcomm, 2018. 20(46): p. 7473–7478.

[21] Tang, T., et al., Composite ZIF-8 with $Cs_3Bi_2I_9$ to Enhance the Photodegradation Ability on Methylene Blue. Molecules, 2025. 30(7): p. 13.

[22] Fan, Q., et al., Solid-state synthesis of lead-free perovskite $Cs_3Bi_2Br_9$ for photocatalytic O_2-involved coupling of aldehydes or alcohols to anhydrides. Journal of Catalysis, 2024. 439: p. 8.

[23] Fernandez-Izquierdo, L., et al., Mechanochemical synthesis of lead-free Perovskites: Comparative kinetics of antimony- and bismuth-based systems. Materials Science in Semiconductor Processing, 2025. 197: p. 9.

[24] Feng, Y., et al., Ligand free synthesis of atomically dispersed Cu doping ultrathin $Cs_3Bi_2Br_9$ for efficient photoreduction CO_2 with high CO selectivity. Applied Catalysis B-Environment and Energy, 2025. 365: p. 12.

[25] Niyitanga, T., et al., Lead-Free $Cs_3Bi_2I_9$ Perovskite-Like Material as Efficient Photocatalyst for Improved Hydrogen Evolution in Presence of Platinum Co-Catalyst. Chemistryselect, 2023. 8(41): p. 9.

[26] He, J., et al., A review of catalytic conversion of carbon dioxide to gas: Applications, challenges, and future development directions. Journal of CO_2 Utilization, 2026. 106: p. 18. Pang, H., T. Masuda, and J. Ye, Semiconductor-Based Photoelectrochemical Conversion of Carbon Dioxide: Stepping Towards Artificial Photosynthesis. Chemistry-an Asian Journal, 2018. 13(2): p. 127–142.

[27] Wang, P., et al., Recent Progress on Photo-Electrocatalytic Reduction of Carbon Dioxide. Particle & Particle Systems Characterization, 2018. 35(1): p. 25.

[28] Liu, Z., et al., $Cs_3Bi_2Br_9/Bi_{19}Br_3S_{27}$ Z-scheme heterojunction for visible-to-near-infrared light-driven photocatalytic CO2 reduction. Journal of Colloid and Interface Science, 2025. 699: p. 9.

[29] Bhosale, S., et al., Mechanism of Photocatalytic CO_2 Reduction by Bismuth-Based Perovskite Nanocrystals at the Gas-Solid Interface. Journal of the American Chemical Society, 2019. 141(51): p. 20434–20442.

[30] Quintero-Lizárraga, O., E. Luévano-Hipólito, and L. Torres-Martínez, A versatile approach for the immobilization of lead-free $Cs_3Bi_2I_9$ perovskites for photocatalytic CO_2 reduction. Journal of Physics D-Applied Physics, 2023. 56(42): p. 9.

[31] Tong, Q., et al., Simultaneous Photocatalytic CO_2 Reduction and H2O Oxidation Under Non-Sacrificial Ambient Conditions. Chemistry-a European Journal, 2024. 30(71): p. 17.

[32] Medina-Llamas, M., et al., Preparation of Heterojunctions Based on $Cs_3Bi_2Br_9$ Nanocrystals and g-C3N4 Nanosheets for Photocatalytic Hydrogen Evolution. Nanomaterials, 2023. 13(2): p. 12.

[33] Xia, Y., et al., Lead-free perovskite $Cs_3Bi_2Br_9/FeS_2$ hollow core-shell Z-scheme heterojunctions toward optimized photothermal-photocatalytic H_2 production. Chinese Chemical Letters, 2025. 36(10): p. 7.

[34] Fan, Y., et al., Enhanced photocatalytic hydrogen evolution through MoS_2 quantum dots modification of bismuth-based perovskites. Chemical Communications, 2024. 60(8): p. 1004–1007.

[35] Alshammari, M., et al., Facilitated charge transfer in a novel rGO-bridged Cs_3Bi_2I9-Sb_2O_3 heterojunction via a s-scheme pathway for sustainable enhanced photocatalytic H_2 production and effective environmental remediation. Surfaces and Interfaces, 2025. 69: p. 16.

[36] Konstantinou, I. and T. Albanis, TiO_2-assisted photocatalytic degradation of azo dyes in aqueous solution: kinetic and mechanistic investigations - A review. Applied Catalysis B-Environment and Energy, 2004. 49(1): p. 1–14.

[37] Chen, C., W. Ma, and J. Zhao, Semiconductor-mediated photodegradation of pollutants under visible-light irradiation. Chemical Society Reviews, 2010. 39(11): p. 4206–4219.

[38] Vijayan, A., et al., Influence of silicon-modified TiO_2 nanocomposites on the photocatalytic degradation of methyl orange and imidacloprid. Zeitschrift Fur Physikalische Chemie-International Journal of Research in Physical Chemistry & Chemical Physics, 2026: p. 31.

[39] Das, G., et al., Valorization of Silk Waste Sericin Through Zinc Oxide Nanoparticles Biosynthesis for Toxic Dye Degradation. Chemistryselect, 2026. 11(9): p. 13.

[40] Bhuvaneswari, M., et al., Silver-polyindole decorated graphitic carbon nitride ($g\text{-}C_3N_4$) nanohybrids for improved pseudocapacitance and photocatalytic degradation of rhodamine B. Ionics, 2026: p. 14.

[41] Akinbami, O., et al., Lead-free Rudorffite-type $Cs_3Bi_2Br_9$ nanoparticles for photocatalytic degradation of rhodamine B and methylene blue. Journal of Photochemistry and Photobiology a -Chemistry, 2021. 419: p. 11.

[42] Bresolin, B., et al., Pb-Free $Cs_3Bi_2I_9$ Perovskite as a Visible-Light-Active Photocatalyst for Organic Pollutant Degradation. Nanomaterials, 2020. 10(4): p. 13.